

A Thomson-type mass and energy spectrometer for characterizing ion energy distributions in a coaxial plasma gun operating in a gas-puff mode

Cite as: Phys. Plasmas **20**, 073115 (2013); <https://doi.org/10.1063/1.4816028>

Submitted: 19 May 2013 . Accepted: 19 June 2013 . Published Online: 29 July 2013

G. B. Rieker, F. R. Poehlmann, and M. A. Cappelli



View Online



Export Citation



CrossMark

ARTICLES YOU MAY BE INTERESTED IN

[Current distribution measurements inside an electromagnetic plasma gun operated in a gas-puff mode](#)

Phys. Plasmas **17**, 123508 (2010); <https://doi.org/10.1063/1.3526603>

[Radial magnetic compression in the expelled jet of a plasma deflagration accelerator](#)

Applied Physics Letters **108**, 094104 (2016); <https://doi.org/10.1063/1.4943370>

[A plasma photonic crystal bandgap device](#)

Applied Physics Letters **108**, 161101 (2016); <https://doi.org/10.1063/1.4946805>

NEW!

Sign up for topic alerts
New articles delivered to your inbox

AIP
Publishing



A Thomson-type mass and energy spectrometer for characterizing ion energy distributions in a coaxial plasma gun operating in a gas-puff mode

G. B. Rieker,^{a)} F. R. Poehlmann,^{b)} and M. A. Cappelli

High Temperature Gasdynamics Laboratory, Stanford University, Stanford, California 94305, USA

(Received 19 May 2013; accepted 19 June 2013; published online 29 July 2013)

Measurements of ion energy distribution are performed in the accelerated plasma of a coaxial electromagnetic plasma gun operating in a gas-puff mode at relatively low discharge energy (900 J) and discharge potential (4 kV). The measurements are made using a Thomson-type mass and energy spectrometer with a gated microchannel plate and phosphor screen as the ion sensor. The parabolic ion trajectories are captured from the sensor screen with an intensified charge-coupled detector camera. The spectrometer was designed and calibrated using the Geant4 toolkit, accounting for the effects on the ion trajectories of spatial non-uniformities in the spectrometer magnetic and electric fields. Results for hydrogen gas puffs indicate the existence of a class of accelerated protons with energies well above the coaxial discharge potential (up to 24 keV). The Thomson analyzer confirms the presence of impurities of copper and iron, also of relatively high energies, which are likely erosion or sputter products from plasma-electrode interactions. © 2013 AIP Publishing LLC. [<http://dx.doi.org/10.1063/1.4816028>]

I. INTRODUCTION

There are a number of applications for the high energy density plasmas that are produced by pulsed coaxial discharge plasma accelerators, including plasma injection into fusion machines,^{1–3} neutron and x-ray production,^{4–6} plasma ion implantation in materials processing,^{7,8} space plasma propulsion,^{9,10} and fusion plasma disruption studies.^{11–13} The most common mode of operation of the coaxial plasma accelerator occurs when the process gases are introduced to the accelerator before the initiation of breakdown. In this so-called “snowplow” mode, a current sheet is formed upon breakdown and propagates along the length of the accelerator due to $\mathbf{J} \times \mathbf{B}$ forces, propelling both the ionized gases and the neutral gases in front of the sheet to high velocities.^{14–16} The collapse of this current sheet just beyond the exit of the accelerator can lead to a strong pinch along the discharge axis that is believed to be the source of highly energetic ions extending into the MeV energy range.¹⁷

Another mode of operation can be accessed if the high voltage is applied across the electrodes before gases are introduced. Breakdown occurs as the gases are injected, forming a stationary ionization zone near the upstream end (breech) of the accelerator followed by a downstream current conducting zone that continuously ionizes the neutral gas as it is injected.^{18–20} In this mode, the gas is concentrated near the breech and the plasma accelerates into vacuum. In analogy to a similar operating mode in chemical combustion, this mode has been introduced by Cheng¹⁸ as the plasma deflagration mode. It is also sometimes referred to as the “high energy mode,”⁵ or as we refer to it here, the “gas-puff mode.” This mode of operation is also believed to lead to the production of energetic ions or energetic plasma of energies

well above the gun discharge potential,⁵ although the mechanism for the production of these ions is less clear.

In a recent paper,²¹ we characterized the dynamics of the current distribution within the interior of a coaxial plasma gun operating in a gas-puff mode to better understand the dynamics of plasma formation and acceleration, and, in particular, the production of these energetic ions. A better understanding of the plasma deflagration mode might enable scaled plasma guns that could provide a high fluence of ions with kinetic energies that are several orders of magnitude higher than those seen in Ref. 5.

Here, we describe the development and application of a Thomson-type mass and energy spectrometer to measure the energy distribution of the high-energy subclass of ions in the accelerated plasma stream, as well as identify and characterize the energy spectra of ionized contaminant species which originate from plasma-electrode interactions. The analyzer uses magnetic and electric fields to disperse ions of different energy and charge-to-mass ratios onto unique trajectories.²² Particles on the different trajectories are detected when they strike a 2D multi-channel plate (MCP) coupled with a phosphor screen. Traditionally, the measured particle trajectories are converted to species-specific energy spectra using a calibration developed by passing particles of a known species and energy through the spectrometer (such as from a calibrated accelerator or particle source [e.g., Ref. 23]), using calculations assuming uniform fields [e.g., Ref. 24], or by placing thin foil sheets of varying thickness in front of the detector designed to filter particles below a set of known threshold energies [e.g., Ref. 25]. In the development of the spectrometer reported here we use Geant4, which is a freely-available Monte Carlo-based toolkit developed for the tracking and interaction of energetic particles with matter.^{26,27} For the purpose of this work, the Monte Carlo-based particle interactions and scattering feature, including secondary particle production, was not employed. Instead, Geant4 was used

^{a)}Present address: Department of Mechanical Engineering, University of Colorado, Boulder, Colorado 80309.

^{b)}Present address: Fluence, LLC, Newark, California 94560.

to design and calibrate the spectrometer by accurately tracking charged particle trajectories through the non-uniform magnetic and electric fields in their precise geometric layout within the spectrometer. To the author's knowledge, this is the first application of Geant4 for calibrating a Thomson-type spectrometer and the first application of the spectrometer to a coaxial plasma accelerator operating in the gas-puff mode.

The following sections in this paper describe the principle of operation, design, and trajectory-based calibration of the spectrometer and present initial results obtained from the coaxial plasma accelerator operating on hydrogen in a deflagration mode with a bank capacitance of $112\ \mu\text{F}$, a transmission line inductance of $50\ \text{nH}$ and an applied electrode voltage of $4\ \text{kV}$. As will be shown, hydrogen ion (proton) energies as high as $24\ \text{keV}$ are detected, confirming that in the gas-puff mode this coaxial discharge provides a mechanism for the production of highly energetic ions at several times the discharge potential.

II. EXPERIMENT

Figure 1 is a schematic of the coaxial plasma gun that is used in the experiments. The coaxial gun is similar to that described in Ref. 28. The outer electrode (anode) has an inner radius of $2.5\ \text{cm}$, while the solid copper inner electrode (cathode) has an outer radius of $2.5\ \text{mm}$. Both electrodes are $23\ \text{cm}$ long. A rod-based design was chosen for the outer electrode to allow visual access to the interior of the plasma gun. The anode consisted of 15 stainless steel rods of $5\ \text{mm}$ diameter that were arranged in a ring with $6.5\ \text{mm}$ gaps between them. A condenser bank consisting of eight capacitors, each with a capacitance of $14\ \mu\text{F}$ and a parasitic inductance of $15\ \text{nH}$, is connected directly to the gun electrodes using $1.75\ \text{m}$ long RG-8 transmission lines, each with a parasitic inductance of approximately $400\ \text{nH}$. No switch was used in the experiments described here to trigger the breakdown process. Instead, the coaxial gun is initially charged to high voltage by exposure to the capacitor bank and the voltage breakdown between the electrodes of the gun is held off on the vacuum side of the Paschen curve. The discharge is then initiated by injecting a hydrogen gas puff from a

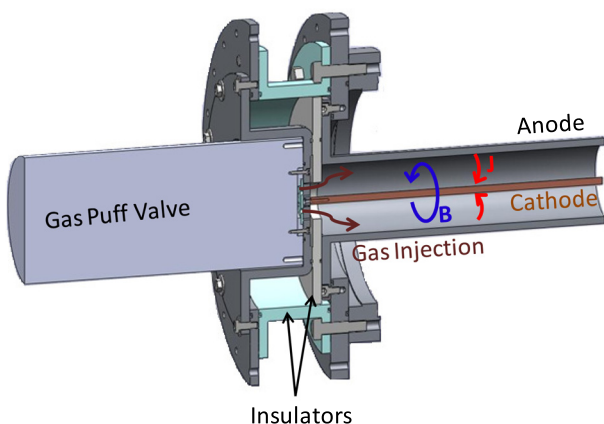


FIG. 1. Schematic of the Stanford coaxial plasma gun with solid anode. Electric current \mathbf{J} gives rise to magnetic field \mathbf{B} . The anode was replaced with fifteen $5\ \text{mm}$ diameter rods for the data shown in Figs. 2, and 7–10.

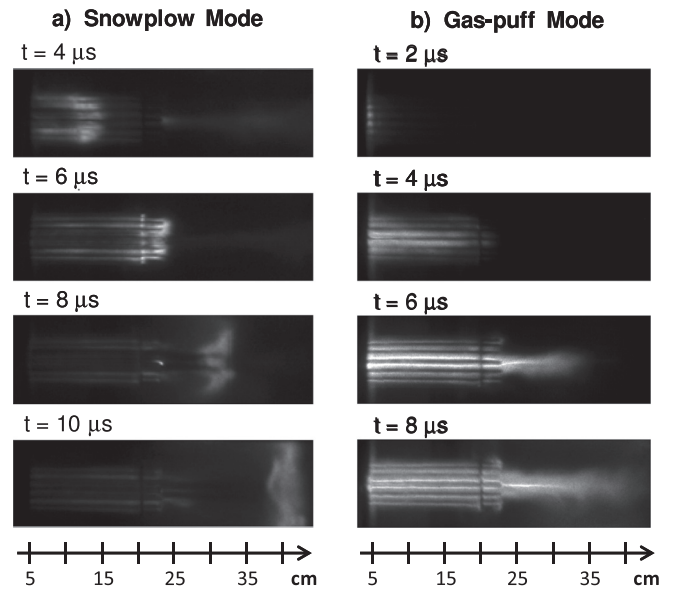


FIG. 2. (After Ref. 28) Fast images of the visible emission during (a) the snowplow mode, and (b) the gas-puff mode of operation in the Stanford coaxial plasma accelerator. Image exposure time = $100\ \text{ns}$, Applied potential = $4\ \text{kV}$, Capacitance = $112\ \mu\text{F}$.

commercially available fast acting gas-puff valve (RM Jordan C-211).

Figure 2 shows short exposure images from the coaxial plasma gun used in these experiments operating in both the snowplow and gas-puff modes. The images reveal the visible emission from the excited plasma. Emission spectrometry of the plasma beam reveals that the emission is primarily from the Balmer series spectral lines of hydrogen. The first $5\ \text{cm}$ of the accelerator are not visible due to accelerator hardware. The two modes are readily distinguished by the difference in the excited plasma front traveling through the accelerator. While the snowplow mode is characterized by a single current sheet traveling along the electrodes, the gas-puff mode is characterized by a distributed current conducting region which eventually comprises the entire length of the electrodes. This is supported by Rogowski coil measurements of the current distribution within the accelerator.²¹ Our results show that two distinct energy subclasses of plasma are emitted from the accelerator. The visible emission in Figure 2 corresponds to the slower-moving bulk plasma, which through time-of-flight estimates is traveling with a proton kinetic energy of $\sim 20\ \text{eV}$. The Thomson spectrometer results reveal a second subclass of particles with proton energies in the several keV range, in some cases with energy several times higher than the applied potential. This subclass is not visible in the fast-framing camera results.

A Thomson-type spectrometer consists of an ion collimator, parallel magnetic and electric fields, and a position-sensitive particle detector.²² After traversing the collimating section, the particles in the ion beam are deflected as they pass through the magnetic field. The trajectory of the individual ions depends on the momentum and charge state of the ion. The ion deflection, x , after traversing a uniform magnetic field of strength B and length L (assuming the Larmor radii of the ions are much larger than the field region, and

small angle deflections), is $x \approx qBL^2/2mv$. Here v , q , and m represent the velocity, charge state, and mass of the ion. It can be seen that slower ions and ions with higher charge state experience greater deflection for a given magnetic field. The ions then pass through a parallel electric field where they are deflected in a direction perpendicular to the deflection from the magnetic field. The magnitude of the deflection depends on the energy and charge state of the ion. The deflection, y , experienced by the ions after traversing a uniform electric field of strength E and length L , is $y \approx qEL^2/2mv^2$ (also assuming small angle deflection). If the fields are co-located, these expressions for the independent deflections can be combined to solve for the relationship between the x and y deflection for an ion of particular mass-to-charge ratio

$$y = \frac{m}{q} \frac{2E}{B^2 L^2} x^2. \quad (1)$$

From Eq. (1), it can be seen that after passing through both fields, particles are deflected onto ‘Thomson parabolas’ in the x - y plane that depend on their mass-to-charge ratio. By detecting the x and y locations of particles that have passed through the fields it is possible to determine the energy, species, and charge state of the particles in the beam, with the exception of ions with the same charge-to-mass ratio (e.g., C^{6+} and O^{8+}), which share the same parabolic trajectories.

Figure 3 shows a schematic of the Thomson spectrometer designed for the present experiments. The spectrometer entrance is located approximately 2 m downstream of the exit of the coaxial plasma gun accelerator in a large vacuum chamber. A grounded skimmer plate with a conical aperture is used to select the center 3 mm of the plasma beam. It is necessary to reject the electrons from the remaining plasma before it passes through the magnetic and electric field regions of the spectrometer so that they do not shield the ions from the fields. This is achieved here by passing the beam through a wire mesh with a grid dimension smaller than the Debye length of the plasma. Under these conditions, the sheath potential that forms at the plasma-mesh interface will block the passage of electrons. The precise plasma temperature and density at the mesh interface is not known, so an estimate of

the worst case (i.e., smallest) Debye length of about $20 \mu\text{m}$ was calculated based on known and estimated properties of the plasma discharge,²⁸ and a grounded $25 \mu\text{m}$ stainless steel mesh was used to reject electrons. The remaining ion beam passes through two 1 mm diameter irises spaced approximately 30 cm apart, which serve to select only the part of the ion beam that is well-collimated at this distance from the accelerator. The 1 mm diameter was selected as a trade-off between signal strength and spectrometer resolution. A smaller diameter collimator leads to higher spectrometer resolution (through narrower Thomson parabolas), but sacrifices particle counts on the detector. The calculation of spectrometer energy resolution is discussed in Sec. III. A final piece of high-density polyethylene shielding with a 1 cm diameter aperture is placed at the entrance to the magnetic field to reject any stray ions left over from the selection process.

The magnetic field is generated by a 15 cm diameter tunable electromagnet. The electric field is provided by two $12 \text{ cm} \times 8 \text{ cm}$ rectangular steel plates located 13.5 cm downstream of the electromagnet. The plates are charged through a $10 \text{ M}\Omega$ resistor with a high voltage power supply (SRS PS350) and stabilized with a 3000 pF blocking capacitor.

The x and y locations of the particles are detected using a 7.5 cm diameter microchannel plate combined with a phosphor screen (Beam Imaging Solutions, BOS-75-IDA). Power for the MCP and phosphor screen is provided by separate high voltage power supplies (SRS PS350). The MCP and phosphor screen power is gated with custom ultra-fast high voltage pull-down switches (Fluence LLC, Newark, CA). The two energy subclasses of particles generated during the $\sim 20 \mu\text{s}$ plasma discharge have different arrival times at the MCP detector. The $> \text{keV}$ subclass is expected to arrive between 1.5 and $24 \mu\text{s}$ after the initiation of the discharge, and the eV subclass starting at $60 \mu\text{s}$. For these experiments, the MCP and phosphor screen were de-energized at $40 \mu\text{s}$ from the initiation of the discharge—after the arrival of the high-energy ion beam but before the arrival of the slower-moving bulk plasma from the discharge. This gating served to protect the MCP assembly against the sudden rise in local pressure and charged particles during the arrival of the bulk plasma. This gating could also be used in the future to gain

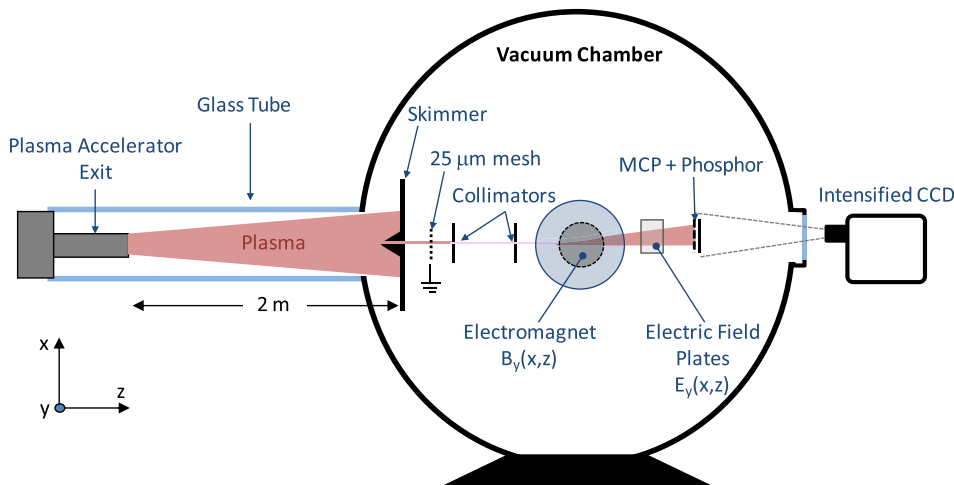


FIG. 3. Schematic of the Thomson-type mass and energy spectrometer.

temporal information about the evolution of high energy particle formation in the plasma accelerator by energizing and de-energizing the MCP assembly during different windows of interest of the plasma pulse.

The phosphor screen was imaged through a window in the vacuum chamber with an intensified CCD. P-43 phosphor was chosen because it offers a high electron-to-photon efficiency and long 1 ms afterglow time (10% afterglow), thus optimizing sensitivity. Though the phosphor is de-energized to prevent further particle strikes after the high energy ion pulse, the afterglow from the original particle strikes continues, so the CCD is set for an exposure time of 2 ms. Phosphors with sub- μ s afterglow are available, and may be useful in the future for time-resolved energy spectra if high-energy particle densities are sufficient to produce detectable signals. Distortion and rotation to the camera image stemming from the optical setup and window were corrected by imaging a square grid at the detector location prior to the experiments and using an image correction algorithm written in Matlab. In this way, the x and y dimensions of the camera images can be accurately scaled directly to the x and y dimensions of the Geant4 simulations of expected particle trajectories (for calibration purposes).

The entire system was aligned to the center axis of the accelerator by removing the center electrode assembly of the accelerator and replacing it with an aligned He-Ne laser assembly. All components of the spectrometer were then aligned relative to the He-Ne beam.

A. Species trajectory calibration

In order to correctly identify the species responsible for each measured Thomson parabola and convert the parabolas into energy spectra for each species, it is necessary to create an accurate map of where particles of various species, charge states, and energy will strike the detector for a given set of magnetic and electric fields. This is most accurately done by calibrating the spectrometer with particles of known species and energy. In practice, this is very difficult since calibrated particle sources or accelerators in the energy range of interest are rarely available. Traditionally, simple trajectory model calculations assuming uniform fields are used for calibration. These calculations do not account for fringe fields and non-uniformity, which can lead to inaccurate energy spectra and makes particle identification difficult in systems with unknown species content.

We chose to approach the problem of calibration using the Geant4 toolkit.^{26,27} This toolkit has been developed over many years by the high energy physics community to simulate the passage of particles through matter. It is possible to re-create the exact geometry of the Thomson spectrometer in the Geant4 environment, including non-uniform fields, and then simulate the passage of charged particles through the spectrometer to create a set of energy calibrations for the measured Thomson parabolas. One additional benefit of the Geant4 toolkit is that it was possible to rapidly iterate on the design of the spectrometer in the Geant4 environment before building any hardware. The size and spacing of the components, and the field strengths were all tuned to meet the desired resolution within the constraints of the available

vacuum chamber, mounting hardware, and the expected output energy range of the accelerator.

While the initial design of the spectrometer was performed assuming uniform fields with no fringe effects, accurate calibration of the spectrometer requires that these effects are included. With the spectrometer built, the actual magnetic field in the y direction (as defined in Figure 3) was measured along the electromagnet radius using a magnetic field probe. An example measurement along the radius is shown in Fig. 4. The measurements show slight non-uniformity in the region between the electromagnet plates, and a fringe field that ranges approximately 5 cm outside of the plates. Measurements at other locations confirmed that the field was radially symmetric, and measurements at other electromagnet currents showed that the field shape was maintained as the field strength was increased. Thus, a single point field strength monitor at the center of the magnet could be used to scale the field at other locations if the magnetic field was adjusted between accelerator pulses. The measurements were used to generate a two dimensional replica of the actual y -direction magnetic field within the Geant4 environment. The magnetic field in the x and z directions (on the center plane between the electromagnet poles) was small and therefore neglected.

Measurements of the non-uniform electric field were more difficult to perform, so simulations were carried out as an alternative. Particles traveling through the electric field region of the spectrometer are deflected from the original beamline in both the x and y directions, therefore, a full three-dimensional (3D) electric field was used in Geant4 based on 3D simulations. Laplace's equation with the boundary conditions shown in Fig. 5 was solved numerically in MATLAB to determine the electric potential for a slice of the high voltage plates in the yz -plane. The magnet structure and detector were represented by simple grounded planes, and the other boundaries of the calculation region were also set at the reference (ground) condition. The electric field in the y and z directions was calculated from the gradient of the electric potential. Because the geometry of the plates is constant in the x direction, the electric field in the x direction is negligible, and the field in the y and z directions can be assumed constant along the x dimension of the electric field plates. A representation of the field in the y and z directions is shown in Fig. 5 to demonstrate the non-uniformity of the fields.

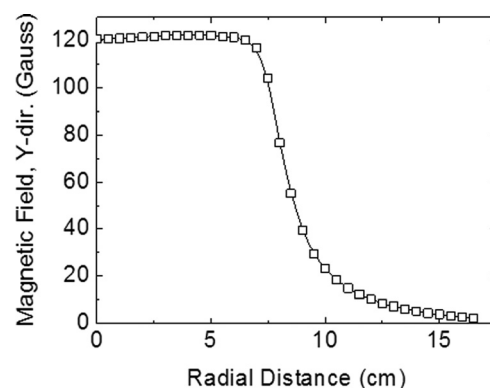


FIG. 4. Magnetic field measurements used for Geant4 simulations.

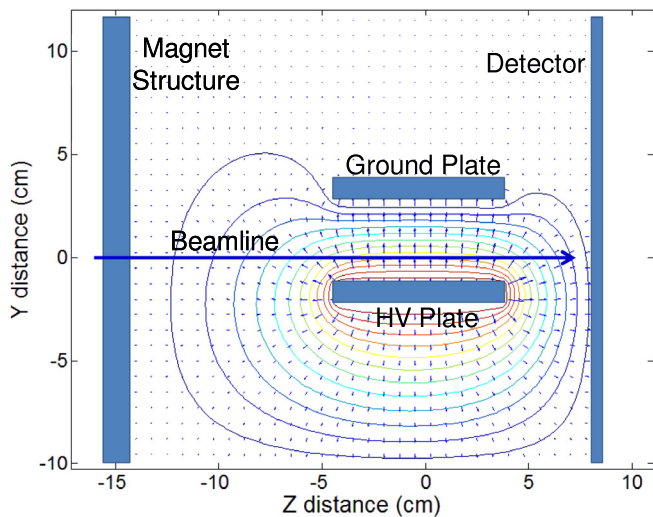


FIG. 5. Electric field calculations used for Geant4 simulations. Contours represent electric potential and vectors represent electric field. The magnet structure, detector, and top and bottom boundaries of the calculation region were assumed to be at the reference (ground) condition.

With the non-uniform fields and complete geometry of the spectrometer represented in Geant4, it was possible to pass particles of various energy and charge-to-mass ratio through the spectrometer to create a calibration for the detector output. It is noteworthy that Geant4 is currently unable to transport partially ionized particles through vacuum environments, and the trajectory results were found to be incorrect for fully ionized particles with atomic number $Z > 1$. However, Geant4 allows the user to specify arbitrary particles, so particles were created with $Z = 1$, and the proper atomic weight for the particle of interest. Then, the magnetic and electric fields were scaled to give the proper trajectory results for other charge states (e.g., double the field strengths to simulate the trajectory of a doubly ionized particle). This method was checked against hand calculations for a simple uniform field situation, and found to be extremely accurate. Figure 6 shows an example Geant4 simulation for protons. The particle trajectories for protons of many different energies are represented by blue lines.

An example Geant4 calibration overlying an image of the MCP detector for a single pulse of the plasma accelerator is shown in Fig. 7. The origin of the Geant4 calibration is aligned with the neutral spot (shown) of the MCP image. This neutral spot is generated by high energy photons and neutral particles which pass unaffected through the magnetic and electric fields of the spectrometer (i.e., x-rays and plasma ions which have recombined before reaching the spectrometer). The neutral spot was shown to be unaffected by magnetic fields up to 0.55 T. Additionally, rotational alignment of the Geant4 and MCP images was achieved using MCP detector images with the electric field of the spectrometer switched off. Under these conditions, particles of all species only exhibit x-deflection, and a single vertical line on the x-axis is visible on the MCP screen. The x-axis of the Geant4 calibration can then be rotated to align with this vertical line on the MCP image, and barring movement of the camera or MCP detector, this rotation can be applied to subsequent images with the electric fields switched on.

Figure 7 also demonstrates the importance of accounting for non-uniformity in the magnetic and electric fields with Geant4, particularly when other contaminant species are present in the beam. The Geant4 overlay shows the simulated Thomson parabolas for protons and C^{6+} under the assumption that the magnetic and electric fields are uniform. Identification of the measured parabola based on these curves would be difficult, and far better agreement is obtained for the proton simulation including non-uniform fields.

To obtain an energy spectrum, the intensity versus x deflection along a measured Thomson parabola must first be extracted (Fig. 8). To do this, the window of the MCP detector image that contains the parabola of interest is first extracted (Fig. 8(a)). The grayscale image is converted to black and white (binary image) by choosing a suitable threshold that eliminates background noise and leaves only the intense pixels of the measured parabola (Fig. 8(b)). A least squares fit of the remaining pixel locations using the general form of Eq. (1) is performed to obtain a curve fit of the Thomson parabola (blue line in Fig. 8(b)). This curve fit is superimposed onto the original image in Fig. 8(c). The intensity of each pixel along the fitted curve is extracted

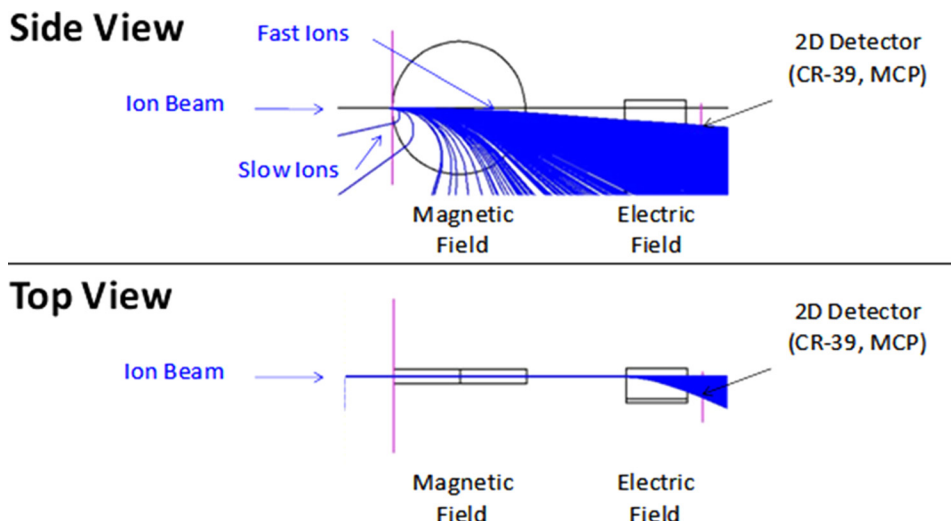


FIG. 6. Example Geant4 simulations for protons of different energies. Ion trajectories are represented by blue curved lines.

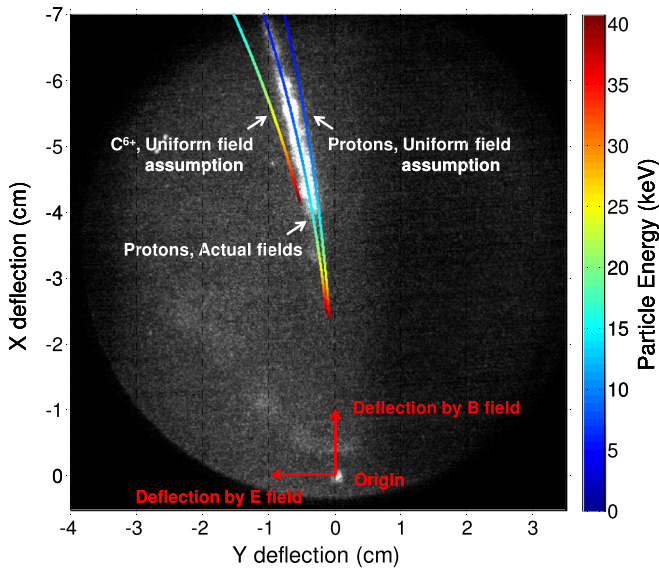


FIG. 7. Image of measured proton Thomson parabola with overlying Geant4 calibration. Incorporating accurate non-uniform magnetic and electric fields improves species identification and calibration accuracy.

(Fig. 8(d)). The grayscale image can also be mean-filtered to reduce noise before extracting the intensities (a mean filter with a 6×6 window was used for the results presented in the figure). Once this extraction is completed, the x -deflection versus energy curve for the Geant4 generated Thomson parabola is used to convert the x deflection along the measured Thomson parabola into particle energy.

III. RESULTS

Figure 9 shows the measured energy spectrum of protons for a single discharge pulse at 4 kV applied voltage and 900 J capacitor bank energy. Protons range from 6 keV to 24 keV (protons of lower energy are deflected outside the

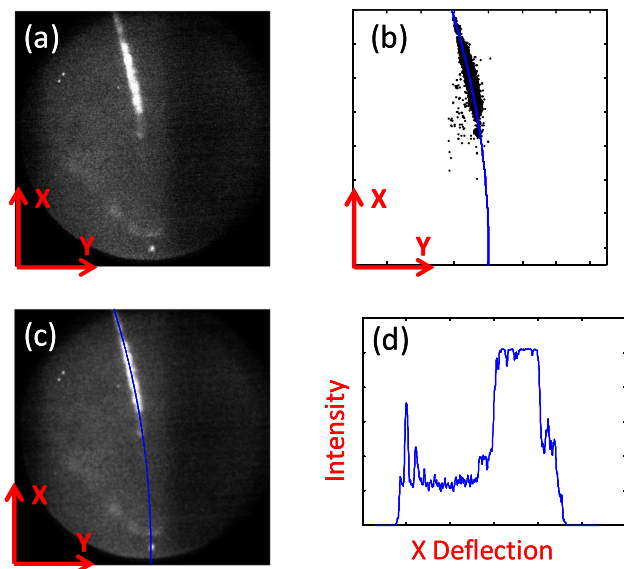


FIG. 8. Image processing to extract Thomson parabolas: (a) original image, (b) conversion to binary image for least-squares fit to Thomson parabola, (c) superimposed fit onto mean-filtered original image, (d) extracted intensity (arbitrary units) along fit parabola.

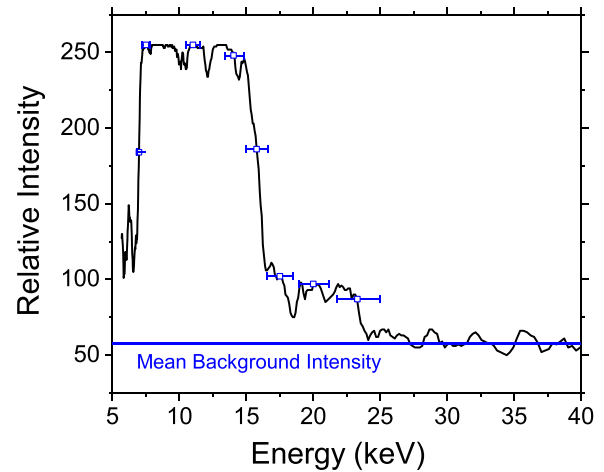


FIG. 9. Proton energy spectrum for single accelerator pulse. 4 kV applied voltage, 900 J capacitor bank energy. Uncertainty bars are shown for select points of the spectrum.

physical extent of the MCP detector), with the highest proton density in the 7.5 to 15 keV range. The intensified camera gain and MCP detector voltage settings were such that the image of the MCP detector is near saturation in the 7.5 keV to 15 keV range. This was done intentionally to increase sensitivity to the high energy wing of the proton signal. Maximum ion energies that are six times the applied voltage indicate that the accelerating mechanism is not the initial electric field between the coaxial electrodes. High energy protons were only detected for approximately 20% of cases with positive high voltage applied to the outer electrode. This may indicate that the acceleration mechanism producing the high energy particles does not occur for each pulse, or that the region is localized and does not occur in the same physical location within the accelerator for each pulse (the spectrometer was only aligned with the center of the accelerator). Furthermore, high energy protons were not detected for any pulse with negative high voltage applied to the outer electrode.

Uncertainty bars are added at select points along the spectrum. Ideally, the plasma beam would be perfectly collimated through a small aperture with no divergence and would result in a thin, intense Thomson parabola measurement. In reality, beam divergence, repulsive forces amongst ions and the need to use a large enough collimator aperture to achieve a detectable MCP signal result in a wider measured Thomson parabola. One can assume that the width of the parabola is a measurement of these combined effects, and sets the energy uncertainty (a sort of energy resolution) of the plasma beam/spectrometer combination. Thus, the width of the Thomson parabola was used to calculate the energy uncertainty at various points along the parabola using the Geant4-generated energy calibration. One can see that the uncertainty increases with energy. This is a result of the nonlinear deflection of ions by the magnetic field. The change in y deflection decreases for increasing energy.

Fig. 10(a) shows the MCP detector image for an accelerator pulse with contaminant species present in the beam. The likely contaminant species are copper (from the inner electrode) or iron (from the outer electrode). The Geant4 overlay

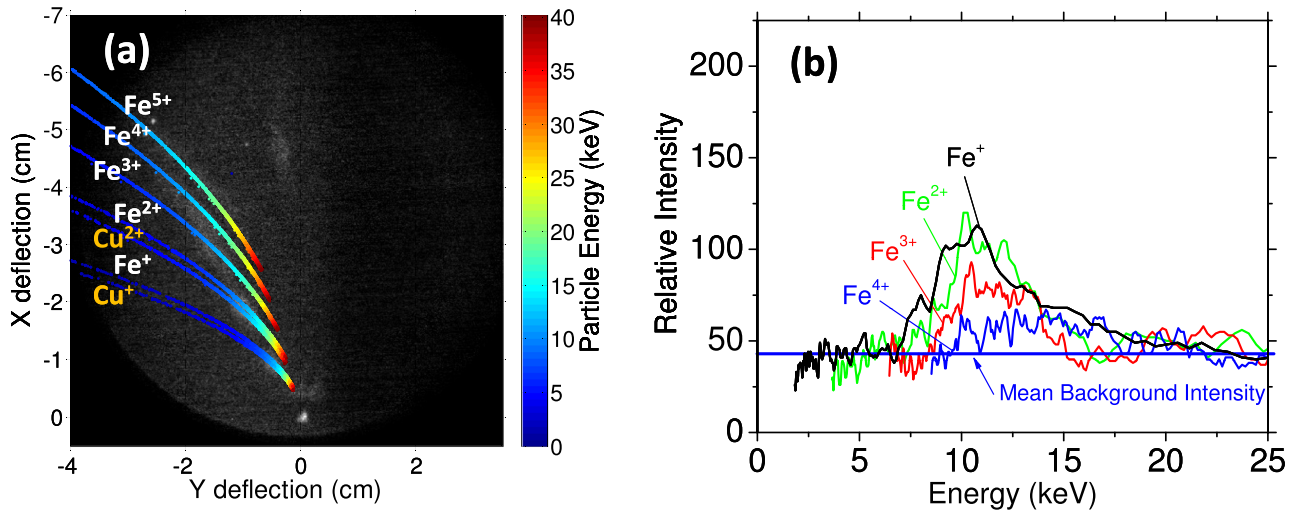


FIG. 10. Left panel: MCP detector image of measured Thomson parabolas with Geant4 calibration overlaid for an accelerator pulse which exhibited contaminant species in the beam. Right panel: Energy spectra for contaminant species, assuming they are various charge states of iron.

shows the Thomson parabolas for the first five ionization states of iron and the first two for copper (to demonstrate the similarity between the two). One can see that given the width of the measured Thomson parabolas, it is not yet possible to distinguish between the contaminant species, but it is likely that both are present in the beam. Fig. 10(b) shows the energy spectra assuming the parabolas are attributable to iron contamination. As expected, the spectra shift to higher energy as ionization state increases. However, the shift is not as great as expected for particles accelerating in an electric field (where doubling the ionization state should double the final energy). This may indicate that particles are accelerated collectively, or that the high field regions that generate these particles are either small in volume or short-lived. It is also interesting to note that the iron/copper contaminants are traveling at lower velocity than the protons, given the similarity of their measured energy ranges but the large difference in mass. Contaminant traces were present in approximately 50% of pulses with positive high voltage applied to the outer electrode. Contaminant traces were present in nearly all pulses with negative high voltage applied to the outer electrode, though protons were not detected for any case of negative high voltage. These results suggest that the species distribution in the accelerator depends on polarity and is most likely affected by the direction of current travel between the electrodes.

IV. SUMMARY

A Thomson-type mass and energy spectrometer was developed and demonstrated for measurements of ion energy spectra and contaminant species identification in a coaxial plasma accelerator operating in the gas-puff mode. The freely available Geant4 toolkit was used to simulate particle trajectories through the non-uniform magnetic and electric fields in their actual geometric configuration within the spectrometer. These trajectories were then used to develop species-specific energy calibrations for the spectrometer. The difference between the uniform field calculations and the full Geant4 calibrations show the importance of these

calculations for accurate species identification and energy spectra extraction.

The spectrometer was used to probe the high-energy subclass of particles generated by the coaxial accelerator. Results show that for hydrogen gas injection, a burst of high-energy protons ranging from 6 keV to 24 keV is produced from an accelerator with 4 kV applied potential and 900 J capacitor bank energy. Shot-to-shot variations in the high-energy proton yield suggest that the acceleration mechanism is either not present during each accelerator pulse or does not occur in the same spatial region from pulse-to-pulse (since the spectrometer only probes the accelerator centerline in these experiments). Additional measurements of the energy spectra of contaminant species originating from the accelerator electrodes show iron and/or copper ions with energies also in the 7 to 20+ keV range. The peak of the energy distributions increases with ionization state but not with the linear relationship expected for acceleration by an electric field. Together, the spectrometer and these results represent an important step toward understanding the acceleration mechanisms for the high-energy subclass of particles in coaxial plasma accelerators operating in the gas-puff mode.

ACKNOWLEDGMENTS

This research was supported by the National Institutes of Health under Award No. 1R21 CA 139320-01, and the Center for Biomedical Imaging at Stanford seed grant program.

¹A. W. Leonard, R. N. Dexter, and J. C. Sprott, *Phys. Rev. Lett.* **57**, 333 (1986).

²S. F. Schaer, *Acta Phys. Pol. A* **88**, S77 (1995).

³S. Woodruff, D. N. Hill, B. W. Stallard, R. Bulmer, B. Cohen, C. T. Holcomb, E. B. Hooper, H. S. McLean, J. Moller, and R. D. Wood, *Phys. Rev. Lett.* **90**, 095001 (2003).

⁴A. Bernard, P. Cloth, H. Conrads, A. Coudeville, G. Gourlan, A. Jolas, C. Maisonnier, and J. P. Rager, *Nucl. Instrum. Methods* **145**, 191 (1977).

⁵J. W. Mather, *Phys. Fluids* **7**, S28 (1964).

⁶F. C. Mejía, M. Milanese, R. Moroso, and J. Pouzo, *J. Phys. D: Appl. Phys.* **30**, 1499 (1997).

- ⁷K. Masugata, Y. Kawahara, C. Mitsui, I. Kitamura, T. Takahashi, Y. Tanaka, H. Tanoue, and K. Arai, in *Power Modulator Symposium, 2002 and 2002 High-Voltage Workshop. Conference Record of the Twenty-Fifth International* (2002), pp. 334–337.
- ⁸P. Yan, P. Hui, W. Zhu, and H. Tan, *Surf. Coat. Technol.* **102**, 175 (1998).
- ⁹M. Y. Wang, C. K. Choi, and F. B. Mead, *AIP Conf. Proc.* **246**, 30 (1992).
- ¹⁰D. Y. Cheng, *AIAA J.* **9**, 1681 (1971).
- ¹¹J. T. Bradley, J. M. Gahl, and P. D. Rockett, *IEEE Trans. Plasma Sci.* **27**, 1105 (1999).
- ¹²V. I. Tereshin, A. N. Bandura, O. V. Byrka, V. V. Chebotarev, I. E. Garkusha, I. Landman, V. A. Makhraj, I. M. Neklyudov, D. G. Solyakov, and A. V. Tsarenko, *Plasma Phys. Controlled Fusion* **49**, A231 (2007).
- ¹³I. E. Garkusha, I. Landman, J. Linke, V. A. Makhraj, A. V. Medvedev, S. V. Mal'khin, S. Peschanyi, G. Pintsuk, A. T. Pugachev, and V. I. Tereshin, *J. Nucl. Mater.* **415**, S65 (2011).
- ¹⁴J. T. Cassidy, Y. C. F. Thio, and S. T. Wu, *Phys. Plasmas* **13**, 053101 (2006).
- ¹⁵P. J. Hart, *J. Appl. Phys.* **35**, 3425 (1964).
- ¹⁶T. D. Butler, I. Henins, F. C. Jahoda, J. Marshall, and R. L. Morse, *Phys. Fluids* **12**, 1904 (1969).
- ¹⁷A. Bernard, H. Bruzzone, P. Choi, H. Chuaqui, V. Gribkov, J. Herrera, K. Hirano, A. Krejci, S. Lee, C. Luo, F. Mezzetti, M. Sadowski, H. Schmidt, K. Ware, C. S. Wong, and V. Zoita, *J. Moscow Phys. Soc.* **8**, 93 (1998).
- ¹⁸D. Y. Cheng, *Nucl. Fusion* **10**, 305 (1970).
- ¹⁹D. M. Woodall and L. K. Len, *J. Appl. Phys.* **57**, 961 (1985).
- ²⁰A. P. Chattock, *Philos. Mag.* **24**, 94 (1887).
- ²¹F. R. Poehlmann, M. A. Cappelli, and G. B. Rieker, *Phys. Plasmas* **17**, 123508 (2010).
- ²²J. J. Thomson, *Philos. Mag.* **21**, 225 (1911).
- ²³S. Ter-Avetisyan, M. Schnürer, S. Busch, E. Risse, P. V. Nickles, and W. Sandner, *Phys. Rev. Lett.* **93**, 155006 (2004).
- ²⁴I. W. Choi, C. M. Kim, J. H. Sung, T. J. Yu, S. K. Lee, I. J. Kim, Y.-Y. Jin, T. M. Jeong, N. Hafz, K. H. Pae, Y.-C. Noh, D.-K. Ko, A. Yogo, A. S. Pirozhkov, K. Ogura, S. Orimo, A. Sagisaka, M. Nishiuchi, I. Daito, Y. Oishi, Y. Iwashita, S. Nakamura, K. Nemoto, A. Noda, H. Daido, and J. Lee, *Rev. Sci. Instrum.* **80**, 053302 (2009).
- ²⁵H. Herold, A. Mozer, M. Sadowski, and H. Schmidt, *Rev. Sci. Instrum.* **52**, 24 (1981).
- ²⁶S. Agostinelli, J. Allison, K. Amako, J. Apostolakis, H. Araujo, P. Arce, M. Asai, D. Axen, S. Banerjee, G. Barrant, F. Behner, L. Bellagamba, J. Boudreau, L. Brogna, A. Brunengo, H. Burkhardt, S. Chauvie, J. Chuma, R. Chytraccek, G. Cooperman, G. Cosmo, P. Degtyarenko, A. Dell'Acqua, G. Depaola, D. Dietrich, R. Enami, A. Feliciello, C. Ferguson, H. Fesefeldt, G. Folger, F. Foppiano, A. Forti, S. Garelli, S. Giani, R. Giannitrapani, D. Gibin, J. J. Gómez Cadenas, I. González, G. Gracia Abril, G. Greeniaus, W. Greiner, V. Grichine, A. Grossheim, S. Guatelli, P. Gumplinger, R. Hamatsu, K. Hashimoto, H. Hasui, A. Heikkinen, A. Howard, V. Ivanchenko, A. Johnson, F. W. Jones, J. Kallenbach, N. Kanaya, M. Kawabata, Y. Kawabata, M. Kawaguti, S. Kelner, P. Kent, A. Kimura, T. Kodama, R. Kokoulin, M. Kossov, H. Kurashige, E. Lamanna, T. Lampén, V. Lara, V. Lefebvre, F. Lei, M. Liendl, W. Lockman, F. Longo, S. Magni, M. Maire, E. Medernach, K. Minamimoto, P. Mora de Freitas, Y. Morita, K. Murakami, M. Nagamatsu, R. Nartallo, P. Nieminen, T. Nishimura, K. Ohtsubo, M. Okamura, S. O'Neale, Y. Oohata, K. Paech, J. Perl, A. Pfeiffer, M. G. Pia, F. Ranjard, A. Rybin, S. Sadilov, E. Di Salvo, G. Santin, T. Sasaki, N. Savvas, Y. Sawada, S. Scherer, S. Sei, V. Sirotenko, D. Smith, N. Starkov, H. Stoecker, J. Sulkimo, M. Takahata, S. Tanaka, E. Tcherniaev, E. Safai Tehrani, M. Tropeano, P. Truscott, H. Uno, L. Urban, P. Urban, M. Verderi, A. Walkden, W. Wander, H. Weber, J. P. Wellisch, T. Wenaus, D. C. Williams, D. Wright, T. Yamada, H. Yoshida, and D. Zschiesche, *Nucl. Instrum. Methods Phys. Res. A* **506**, 250 (2003).
- ²⁷J. Allison, K. Amako, J. Apostolakis, H. Araujo, P. A. Dubois, M. Asai, G. Barrant, R. Capra, S. Chauvie, R. Chytraccek, G. A. P. Cirrone, G. Cooperman, G. Cosmo, G. Cuttone, G. G. Daquino, M. Donszelmann, M. Dressel, G. Folger, F. Foppiano, J. Generowicz, V. Grichine, S. Guatelli, P. Gumplinger, A. Heikkinen, I. Hrivnacova, A. Howard, S. Incerti, V. Ivanchenko, T. Johnson, F. Jones, T. Koi, R. Kokoulin, M. Kossov, H. Kurashige, V. Lara, S. Larsson, F. Lei, O. Link, F. Longo, M. Maire, A. Mantero, B. Mascialino, I. McLaren, P. M. Lorenzo, K. Minamimoto, K. Murakami, P. Nieminen, L. Pandola, S. Parlati, L. Peralta, J. Perl, A. Pfeiffer, M. G. Pia, A. Ribon, P. Rodrigues, G. Russo, S. Sadilov, G. Santin, T. Sasaki, D. Smith, N. Starkov, S. Tanaka, E. Tcherniaev, B. Tome, A. Trindade, P. Truscott, L. Urban, M. Verderi, A. Walkden, J. P. Wellisch, D. C. Williams, D. Wright, and H. Yoshida, *IEEE Trans. Nucl. Sci.* **53**, 270 (2006).
- ²⁸F. R. Poehlmann, "Investigation of a plasma deflagration gun and magnetohydrodynamic Rankine-Hugoniot model to support a unifying theory for electromagnetic plasma guns," Ph.D. thesis (Stanford University, 2010).